International Journal of Coal Geology 219 (2020) 103371

Contents lists available at ScienceDirect

International Journal of Coal Geology

journal homepage: www.elsevier.com/locate/coal

Speciation transformation of rare earth elements (REEs) during heating and implications for REE behaviors during coal combustion

Pan Liu[a], Lufeng Yang[b], Qian Wang[a], Biao Wan[a], Qing Ma[c], Hailong Chen[b,*], Yuanzhi Tang[a,*]

[a] School of Earth and Atmospheric Sciences, Georgia Institute of Technology, 311 Ferst Dr, Atlanta, GA 30332-0340, USA
[b] Woodruff School of Mechanical Engineering, Georgia Institute of Technology, 771 Ferst Dr, Atlanta, GA 30332-0245, USA
[c] DND-CAT, Northwestern Synchrotron Research Center at the Advance Photon Source, 9700 S Cass Ave, Lemont, IL 60439, USA

ARTICLE INFO

Keywords:
Rare earth elements
Coal combustion
Coal ash
Mineral transformation
XAS

ABSTRACT

The recovery of rare earth elements (REEs) from coal ash has gained growing attention as a promising resource recovery strategy. Compared to extensive studies on REE occurrence in coal and coal ash, few studies have investigated REE behaviors during coal combustion processes. This study investigated the mineralogy, oxidation state, and structure changes of twelve representative REE-bearing phases during heating up to 1500 °C using complementary thermal analysis, in-situ X-ray diffraction (XRD), scanning electron microscopy (SEM), and X-ray absorption spectroscopy (XAS), in order to better understand and predict REE behaviors during coal combustion processes. It was found that: (1) REE-lignin and REE-chitosan complexes, hydrated $Y_2(CO_3)_3$ and $Ce_2(CO_3)_3$, bastnäsite, and REE-doped calcite transformed to corresponding oxides after heating, accompanied by Ce(III) oxidation; (2) hydrated YPO_4 and $CePO_4$ formed corresponding anhydrous REE phosphates after heating with no evident Ce(III) oxidation; and (3) apatite, monazite, xenotime, and zircon barely altered during heating, although Ce(III) in apatite was partially oxidized and Y local structure became more disordered in apatite, monazite, and zircon. These results are consistent with previous studies on REE speciation in coal and coal ash and provided an in-depth understanding on REE behaviors during coal combustion, including mineral transformations and retention of REE-bearing phases. XAS analysis revealed that due to the co-existence of different REEs, mineralogical changes, and local structural distortion of REE-bearing phases during combustion, quantification of REE speciation in coal ash using XAS should be interpreted with caution and cross-validated by other techniques.

1. Introduction

Rare earth elements (REEs, including lanthanides and yttrium) are labeled as “critical materials” because of their importance for modern economy and the potential risks of supply disruptions (Long et al., 2012; Blissett et al., 2014). Over the recent years, there are growing interests in developing cost effective and environmentally friendly techniques for domestic recovery of REEs (Liang et al., 2016; Maes et al., 2017; Park et al., 2017). Coal combustion products such as coal ash (CA) have been suggested to be a promising REE source (Seredin and Dai, 2012; Franus et al., 2015; Taggart et al., 2016; Dai and Finkelman, 2018), since REEs are concentrated in CA at an average total concentration of ~500 ppm after coal combustion processes (Taggart et al., 2016).

In order to develop effective approaches for REE extraction from CA, many previous studies have investigated the chemical speciation and physical distribution of REEs in CA (e.g., Hood et al., 2017; Kolker et al., 2017; Hower et al., 2018; Montross et al., 2018; Stuckman et al., 2018; Taggart et al., 2018; Liu et al., 2019) and raw feed coal (e.g., Lin et al., 2017; Dai and Finkelman, 2018). Results from those studies revealed that REE-bearing phases might undergo varied degrees of speciation change and re-distribution during coal combustion. For example, REE-bearing phases (e.g., monazite and zircon) displayed morphological characteristics of spherical shape (Liu et al., 2019) and size reduction (Hood et al., 2017) as observed by scanning electron microscopy (SEM). In addition to the occurrence of REE-bearing particles encapsulated in aluminosilicate glass phase (e.g., Hower et al., 2018; Stuckman et al., 2018; Liu et al., 2019), REEs were also found to be dispersed throughout glass, likely resulting from the decomposition of REE-bearing phases and mobilization into glass (e.g., Kolker et al., 2017; Stuckman et al., 2018; Liu et al., 2019). Moreover, most REEs are generally present at trivalent oxidation state, while Ce can occur as

* Corresponding authors.
E-mail addresses: hailong.chen@me.gatech.edu (H. Chen), yuanzhi.tang@eas.gatech.edu (Y. Tang).

https://doi.org/10.1016/j.coal.2019.103371
Received 8 August 2019; Received in revised form 30 October 2019; Accepted 14 December 2019
Available online 14 December 2019
0166-5162/

both Ce(III) and Ce(IV). Using micro X-ray absorption spectroscopy (μ-XAS), Stuckman et al. (2018) found 10-μm Ce(IV) oxides and partially oxidized Ce-bearing particles in CA, which might have resulted from the decomposition and oxidation of REE-bearing phases during coal combustion.

The retention and/or transformation of REEs are likely dependent on factors such as the thermal stability of REE-bearing phases, boiler temperature, and exposure to untreated flue gas after combustion. Coal is generally combusted at temperatures ranging from 1200 to 1800 °C (Quann et al., 1982) in 20% excess air (Wall et al., 2009). These temperatures are higher than the decomposition point of some REE-bearing phases, potentially resulting in REE speciation changes during combustion. Additionally, in oxidizing atmosphere, Ce(III) might be oxidized by O_2 to form Ce(IV)-containing species such as $Ce^{IV}O_2$. After combustion, REEs are exposed to untreated flue gas with a temperature gradient from 1400 °C to 60–150 °C (Stuckman et al., 2018). The flue gas can contain ~73% N_2, 15–16% CO_2, 5–7% H_2O, and 3–4% O_2, and trace amounts of SO_x (up to 800 ppm) and NO_x (up to 500 ppm) (Granite and Pennline, 2002), which might react with REEs to form REE carbonates or sulfates (Stuckman et al., 2018).

Previous studies on REE speciation focused either on feed coal or CA with no systematical investigations on the behaviors of REE-bearing phases during coal combustion. Understanding the fate of REEs during coal combustion would not only contribute to improved understandings of REE speciation and distribution in CA, but also provide a knowledge basis for modeling REE transformation during combustion processes and for exploring proper pretreatment methods (e.g., calcination, Zhang and Honaker, 2019) to improve REE recovery from coal and CA.

Additionally, synchrotron-based spectroscopy techniques such as bulk and micro XAS have been widely applied to identify and quantify REE speciation in CA (Stuckman et al., 2018; Taggart et al., 2018; Liu et al., 2019). However, the potential mineralogical and structural changes of REE-bearing phases during coal combustion pose challenges on the reliability of XAS results, since pure and pristine REE reference compounds were typically used for data processing (e.g., linear combination fitting of XAS spectra) in these previous studies. Thus, it is also critical to investigate the behaviors of REEs during coal combustion in order to provide guidance for the choice of REE reference compounds and for data interpretation.

The goal of this study is to investigate the behaviors of representative REE-bearing phases during coal combustion processes. Thermal analysis and in-situ X-ray diffraction (XRD) were combined with complimentary techniques such as SEM and XAS to characterize the mineralogical, morphological, oxidation state, and structural changes of REE-bearing phases. Representative REE-bearing phases identified in feed coal or CA were chosen for this study, including REE-organic complexes (Lin et al., 2017; Laudal et al., 2018), REE carbonates and REE-bearing calcite (Dai et al., 2014; Montross et al., 2018), REE phosphates (Hower et al., 2018; Liu et al., 2019), apatite (Liu et al., 2019), and zircon (Hood et al., 2017; Liu et al., 2019). The results obtained in this study are further compared with previous studies, and can provide an in-depth understanding on REE transformation during coal combustion processes.

2. Materials and methods

2.1. REE-bearing phases

Twelve (12) REE-bearing phases were obtained or synthesized for this study (Table 1). Chemicals of ACS grade or higher were used for the synthesis of REE-bearing phases. Synthesis and characterization of most of these compounds have been described in our recent study (Liu et al., 2019). Among all the REE elements, Ce and Y were chosen as "probes" for light REEs (LREEs, La−Sm) (Stuckman et al., 2018) and heavy REEs (HREEs, Eu−Lu) (Taggart et al., 2018; Liu et al., 2019), respectively.

REE-organic complexes included REE-lignin and REE-chitosan complexes. Lignin and chitosan were chosen since they are natural biopolymers and important substances for coal formation (Hatcher et al., 1982; Goodarzi, 1984). REE-lignin or REE-chitosan complexes was prepared by adding 0.5 g lignin or chitosan into a 20 mL solution containing 100 μM each of $CeCl_3$, $NdCl_3$, and YCl_3 (Sigma-Aldrich, 99.99% trace metal basis) at pH 7 with agitation, followed by filtration and freeze drying. Hydrated Y and Ce carbonates (99.99% trace metal basis) were purchased from Sigma-Aldrich. REE-doped calcite was synthesized following a constant-addition method (Tang et al., 2007). Briefly, 0.05 M $CaCl_2$ and 0.05 M $NaHCO_3$ solutions were pumped separately at a rate of 150 μL/min into a stirred reaction vessel with continuous air bubbling. The reaction vessel contained 700 mL freshly-prepared solution with 5 mM $CaCl_2$, 5 mM $NaHCO_3$, and 0.1 M NaCl as background electrolyte and 15 μM each of $CeCl_3$, $NdCl_3$, and YCl_3. After 6 h reaction, the pH stabilized at 8.2, and the solid precipitates were harvested using vacuum filtration, rinsed with deionized water (DI), and freeze-dried. Hydrated $CePO_4$ and YPO_4 were synthesized by co-precipitation of $CeCl_3$ or YCl_3 solution with H_3PO_4 solution at a molar ratio of 1:10 (Lucas et al., 2004b). The solution was stirred overnight and the solid precipitates were filtered, rinsed with DI water, and freeze dried. Bastnäsite, monazite, xenotime, apatite, and zircon are natural minerals (personal collection) (Table 1) and their phase purity was confirmed by XRD. Although bastnäsite is relatively rare in coal, it is included to represent natural REE-carbonate minerals in coal.

2.2. Analytical methods

2.2.1. Thermal analysis

Simultaneous thermogravimetric and differential scanning calorimetry (TGA-DSC) measurements were conducted on a SDT-Q600 (TA instruments). Certified standards were used for calibration before sample measurements. About 30 mg samples were loaded into an alumina pan and heated from room temperature to 1500 °C (the highest temperature that can be achieved using this instrument) at a heating rate of 20 °C/min and air flow of 100 mL/min (oxidizing atmosphere). After the temperature was held at 1500 °C for 10 min, samples were cooled down to room temperature with forced air flow, which took ~45 min. The reacted samples were finely ground and stored at room temperature for further characterizations by SEM and XAS.

2.2.2. In-situ X-ray diffraction (XRD)

The mineralogical changes of samples during heating and cooling were investigated by in-situ XRD using a Bruker D8 Advanced diffractometer (Mo target, λ = 0.709 Å) coupled with a HTK1200N temperature controlling chamber. Sample pellets were heated from room temperature to 1000 °C (the highest temperature that can be achieved using this apparatus) and then cooled down at a rate of 25 °C. Samples were heated in air (oxidizing atmosphere). During heating and cooling, temperature was held constant at 30, 300, 700, and 1000 °C for 1 h, during which XRD patterns were collected at 3.5–40° 2θ with a step size of 0.016° 2θ and a contact time of 1.5 s/step.

2.2.3. Scanning electron microscopy and energy dispersive X-ray spectroscopy (SEM-EDX)

The morphological characteristics of samples before and after heating to 1500 °C by TGA-DSC were investigated by a Hitachi SU8230 SEM. Samples were dusted on carbon tapes and imaged at 5 kV and 10 μA with a working distance of 5 mm. For chemical composition analysis, EDX spectra (Oxford X-Max^N EDX) were collected at 30 kV and 30 μA with a working distance of 15 mm and contact time of > 1 min.

2.2.4. X-ray absorption spectroscopy (XAS)

Y K-edge and Ce L_{III}-edge XAS spectra of REE-bearing phases before and after heating to 1500 °C by TGA-DSC were collected at Beamline 5-BM-D at the Advanced Photon Source (APS, Lemont, IL) using Si(111) monochromator. The monochromator was detuned 40% to avoid higher

Table 1
Summary on the mineralogy and oxidation state changes of REE-bearing phases after heating up to 1500 °C.

Category	REE-bearing phase	Changes after heating	
		Phase transformation	Oxidation state
REE- organic complexes	REE-lignin	REE-lignin → Y_2O_3	Ce(III) → Ce(IV)
	REE-chitosan	REE-chitosan → CeO_2	Ce(III) → Ce(IV)
REE carbonates	Hydrated $Y_2(CO_3)_3$	Hydrated $Y_2(CO_3)_3$ → Y_2O_3	NA
	Hydrated $Ce_2(CO_3)_3$	Hydrated $Ce_2(CO_3)_3$ → CeO_2	Ce(III) → Ce(IV)
	bastnäsite	(Ce, La)CO_3(F, OH) → (Ce, La)O_2	Ce(III) → Ce(IV)
REE-bearing carbonates	REE-doped calcite	$CaCO_3$ → CaO	Ce(III) → Ce(IV)
REE phosphates	hydrated YPO_4	YPO_4•$2H_2O$ → YPO_4	NA
	hydrated $CePO_4$	$CePO_4$•H_2O → $CePO_4$	No change
	monazite	No change	No change
	xenotime	No change	No change
REE-bearing phosphates	Apatite	No obvious change	Partial oxidation of Ce(III)
REE-bearing silicates	zircon	No change	Likely no change[a]

[a] Ce L_{III}-edge XANES spectra of zircon before and after heating were not obtained due to low concentration of Ce in this zircon sample. However, similar to monazite and xenotime, it is highly likely that Ce in zircon would not be oxidized during heating.

order harmonics. Powdered samples were packed into an acrylic sample holder for data collection. X-ray absorption near edge structure (XANES) spectra were collected. Hydrated $Y_2(CO_3)_3$ and $Ce_2(CO_3)_3$ were used for energy alignment, and their spectra were collected in the reference channel simultaneously with sample scans. XAS data was processed using the software Ifeffit (Ravel and Newville, 2005). Energy alignment was conducted using the reference channel (hydrated $Y_2(CO_3)_3$ at 17056.5 eV for Y K-edge and $Ce_2(CO_3)_3$ at 5726.5 eV for Ce L_{III}-edge). Multiple (2–8) scans were collected, aligned, and averaged for each sample.

3. Results

The combined results from TGA-DSC, in-situ XRD, SEM-EDX, and XANES were used to investigate the behaviors of REE-bearing phases during heating. SEM-EDX analysis was conducted on REE-bearing phases before and after TGA-DSC analysis, while in-situ XRD was used to study the in-situ mineral changes of REE-bearing phases during heating and cooling. The highest temperatures that the TGA-DSC (1500 °C) and in-situ XRD (1000 °C) could reach in this study were slightly lower than the average temperature of coal combustion at 1200–1800 °C. However, the mineralogical changes of most REE-bearing phases occurred at temperatures well below 1000 °C based on TGA-DSC and in-situ XRD (see Section 3.1), therefore our experimental approaches were capable of tracing the mineralogical changes of REE-bearing phases. Based on the EDX results, the chemical composition of REE-bearing phases after TGA-DSC were not distinct from that of pristine ones, likely due to the non-volatile nature of REEs and intrinsic insensitivity of EDX to volatile elements (e.g., H and C).

Overall, based on the combined results from TGA-DSC, in-situ XRD, and SEM-EDX, the behaviors of REE-bearing phases during heating can be divided into three groups and are presented in Section 3.1. Y and Ce XAS spectra of REE-bearing phases before and after TGA-DSC analysis were also collected, which provided information on REE local structure and oxidation states and are presented separately in Section 3.2.

3.1. In-situ XRD, SEM-EDX, and TGA-DSC analyses

3.1.1. REE-lignin and REE-chitosan complexes

Pristine REE-lignin complex showed a strong reflection at 2.81 Å in d-spacing, while a broad reflection at 4.23 Å was observed for pristine REE-chitosan complex along with a series of reflections at 3.44, 2.55, 2.09, and 1.60 Å from the sample holder (corundum, Al_2O_3, PDF# 46–1212) (Fig. 1a and b). In SEM images, REE-lignin complex occurred as irregular aggregates with particle sizes at 1–20 μm (Fig. 2a), while REE-chitosan complex displayed a flaky shape with larger particle sizes (50–200 μm) (*Supporting Information*, SI, Fig. S1a). Based on EDX results, REE-lignin complex was more enriched in Y, while REE-chitosan complex was enriched in Ce and Nd. Differences in REE enrichment are likely due to the intrinsic differences in affinity of different REEs to organics (Wood, 1993).

As shown in Fig. 3a, the decomposition of REE-lignin complex during heating was characterized with four steps of weight loss. The first weight loss (~12%) at around 100 °C was likely due to dehydration, an endothermic process, while the rest stepwise weight loss (a total of ~76%) at 300–900 °C were from combustion, a typical exothermic process. In-situ XRD results (Fig. 1a) show that the dehydration process was not associated with any mineralogical changes, while yttriaite (Y_2O_3, PDF# 25–1200) began to form after 300 °C. The newly-formed yttriaite from REE-lignin complex after heating had a small particle size (~5 μm) and porous texture (Fig. 2a).

The TGA and DSC curves of REE-chitosan complex were similar to that of pure chitosan (Fig. 3b), with the first weight loss/endothermic peak from the loss of water (50–200 °C) and the second weight loss/exothermic peak (300–600 °C) due to depolymerization and combustion in air (Peniche-Covas et al., 1993). XRD pattern of REE-chitosan complex started to change at 300 °C, at which temperature no reflections were observed except for those from the sample holder (Fig. 1b). Cerianite (CeO_2, PDF# 43–1002) first appeared at 700 °C with a strong reflection at 3.12 Å in d-spacing. The produced cerianite (after TGA-DSC analysis) was characterized with a porous texture with nano-sized spherical particles on the surface (Fig. S1a).

3.1.2. Hydrated $Y_2(CO_3)_3$ and $Ce_2(CO_3)_3$

The purchased hydrated $Y_2(CO_3)_3$ was Y-tengerite ($Y_2(CO_3)_3$•$2-3H_2O$, PDF# 24–1419), and the hydrated $Ce_2(CO_3)_3$ was consisted of kozoite ((REE)CO_3(OH)•xH_2O) and Ce-lanthanite ($Ce_2(CO_3)_3$•$8H_2O$, PDF# 38–0377) (Fig. 1c and d). XRD reference of kozoite is not available in the database, but reflections such as those at 4.30, 3.69, 2.95, and 2.35 Å in d-spacing were consistent with reported d-values of (110, 020), (111, 021), (121, 102), and (131) of natural Nd-kozoite, respectively (Miyawaki et al., 2000). Hydrated $Y_2(CO_3)_3$ and $Ce_2(CO_3)_3$ had small particle sizes (generally < 5 μm) and typically occurred as aggregates (Figs. S1b and c).

The decomposition of hydrated $Y_2(CO_3)_3$ was a complex process with at least four stages of weight loss and four corresponding endothermic peaks centered at 170, 300, 470, and 540 °C (Fig. 3c). The weight stabilized at 44.7 wt% after 700 °C. Previous study showed that such a process involved continuous loss of H_2O and CO_2, formation of intermediates (e.g., $YO_{1.1}(CO_3)_{0.4}$), and final formation of Y_2O_3 (Fedorov and Il'in, 2012). In-situ XRD results confirmed the transformation of Y-tengerite into a new phase at 300 °C (the intermediates) and the formation of Y_2O_3 (PDF# 25–1200) at 700 °C (Fig. 1c). Due to

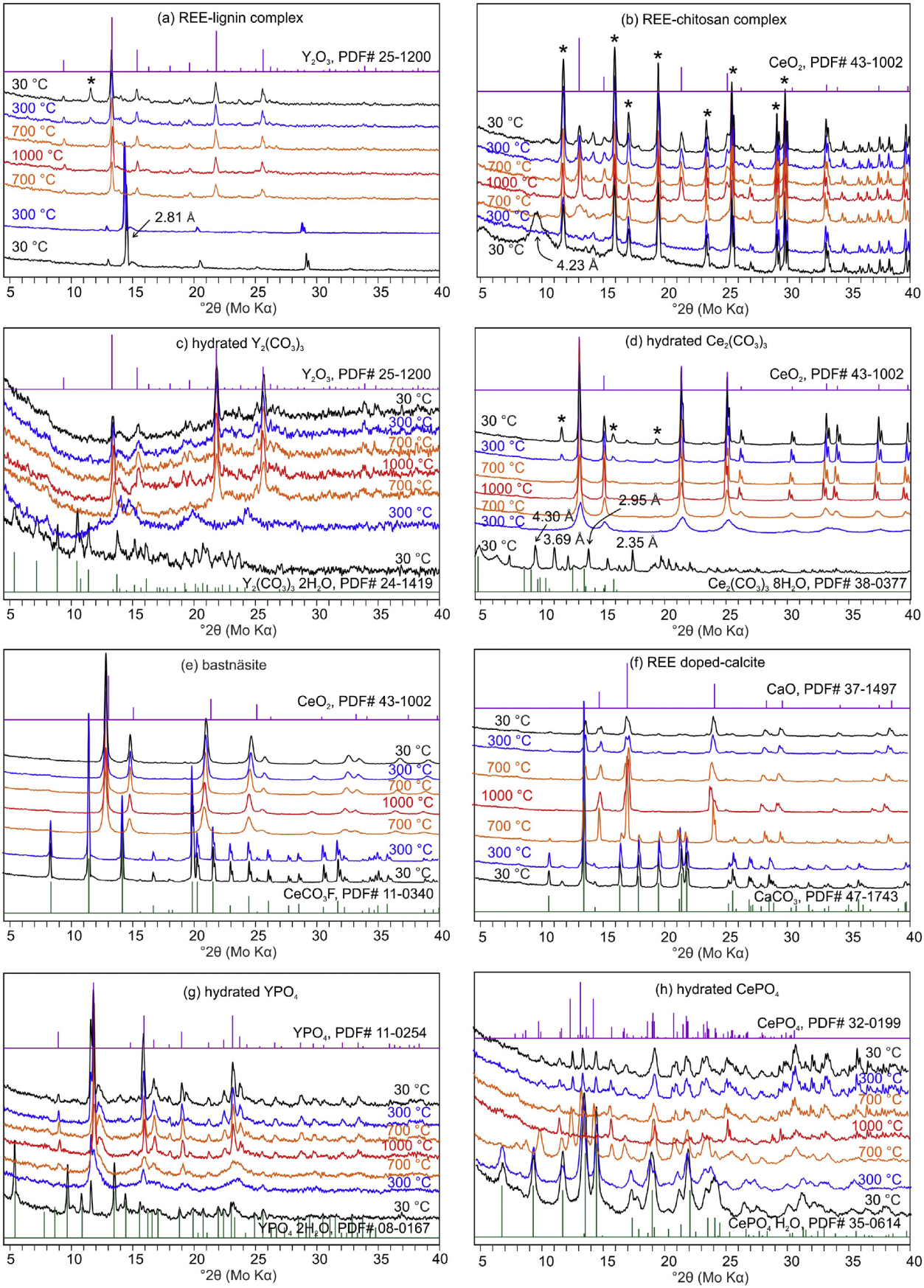

Fig. 1. In-situ XRD patterns of REE-bearing phases during heating and cooling. In each panel, XRD patterns from bottom to top were collected at 30 °C (pristine), during heating (at 300, 700, and 1000 °C), and during cooling (at 700, 300, and 30 °C). Reflection peaks marked with * are from the sample holder (corundum (Al_2O_3), PDF# 46–1212) due to significant phase decomposition.

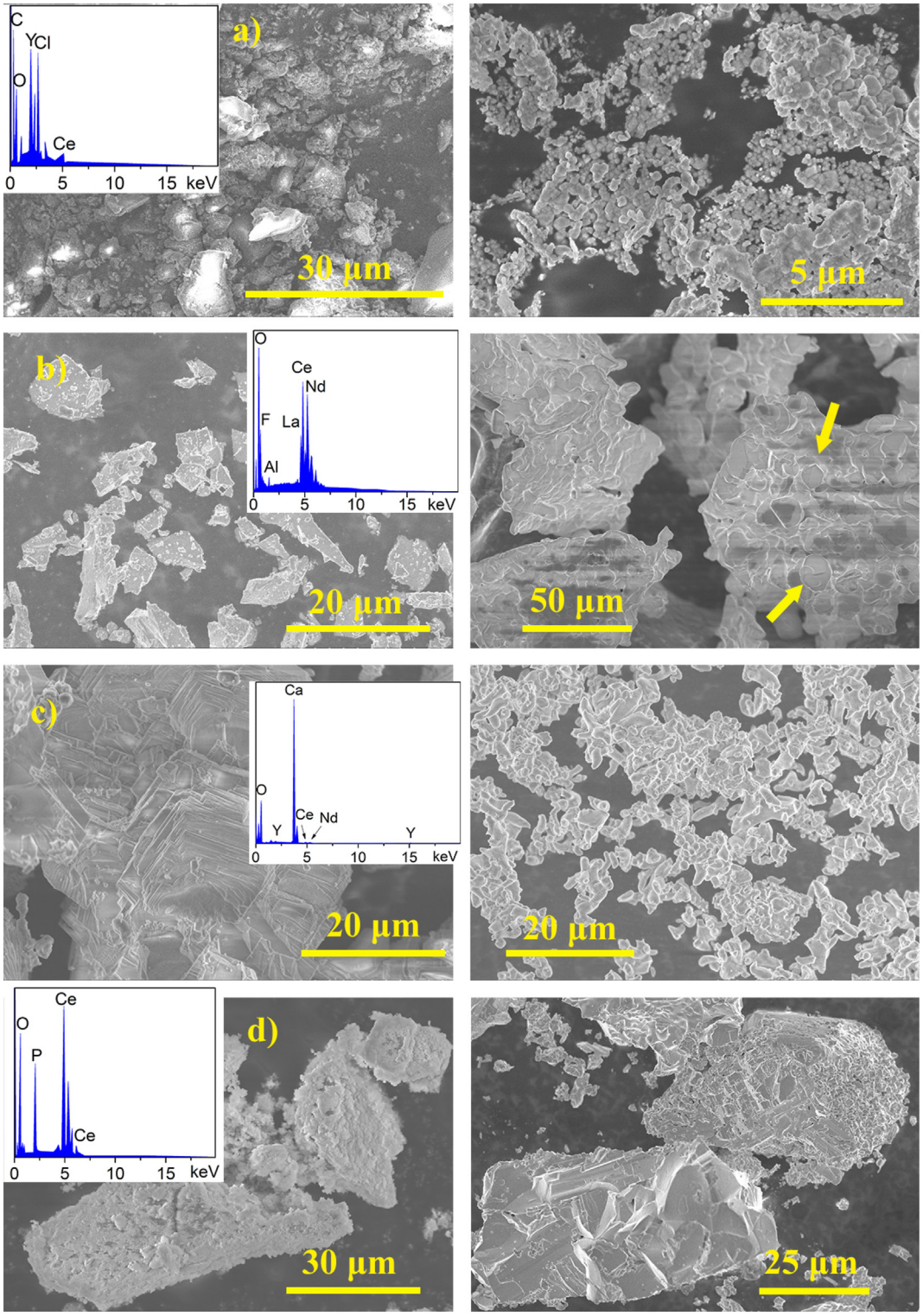

Fig. 2. Representative SEM images showing REE-bearing phases before (left panels) and after (right panels) heating to 1500 °C by TGA-DSC. Inserts show the corresponding EDX spectra of pristine REE-bearing phases. (a) REE-lignin, (b) bastnäsite, (c) REE-doped calcite, and (d) hydrated $CePO_4$. Yellow arrows in (b) indicate two crystalline particles, which might be cerianite (CeO_2) as shown in Fig. 1e by XRD. (For interpretation of the references to colour in this figure legend, the reader is referred to the web version of this article.)

the small particle size, morphologies of pristine hydrated $Y_2(CO_3)_3$ and the product were not distinctively different (Fig. S1b).

Although the hydrated $Ce_2(CO_3)_3$ in this study was a mixture of Ce-lanthanite and kozoite, its decomposition process was relatively simple and consistent with a previous study (Padeste et al., 1994). There were two steps involved: the first step (centered at 150 °C) was due to the loss of H_2O and the second stage (centered at 315 °C) from the generation of CO_2 and the formation of CeO_2 (Fig. 3d) (Padeste et al., 1994). In line with the TGA-DSC results, in-situ XRD showed that a new phase formed at 300 °C, and its XRD reflections matched with cerianite (CeO_2, PDF# 43–1002) (Fig. 1d). In SEM images, newly-formed CeO_2 displayed a porous texture, and some particles appeared to have a hexagonal shape

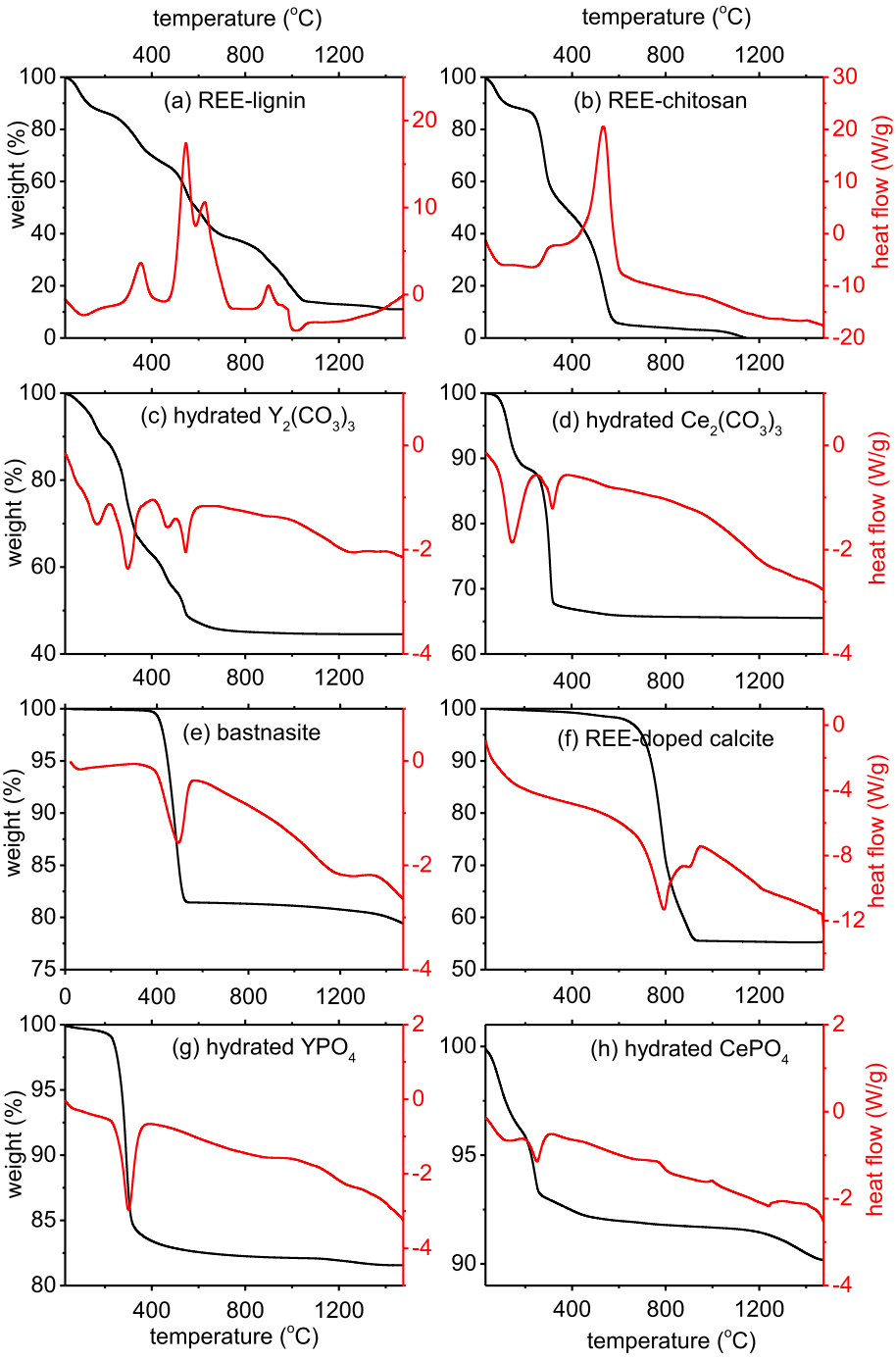

Fig. 3. TGA (black lines) and DSC (red lines) measurements of REE-bearing phases during heating: (a) REE-lignin, (b) REE-chitosan, (c) hydrated $Y_2(CO_3)_3$, (d) hydrated $Ce_2(CO_3)_3$, (e) bastnäsite, (f) REE-doped calcite, (g) hydrated YPO_4, and (h) hydrated $CePO_4$. (For interpretation of the references to colour in this figure legend, the reader is referred to the web version of this article.)

(Fig. S1c).

3.1.3. Bastnäsite

Bastnäsite was confirmed by XRD as a pure phase (PDF# 11–0340) (Fig. 1e), and SEM-EDX results showed that it had a particle size of > 20 μm and was enriched in LREEs (Fig. 2b). The decomposition of bastnäsite was characterized with a single weight loss stage and endothermic peak mainly from the generation of CO_2 (Fig. 3e). Bastnäsite began to decompose at 400 °C with a maximum at 500 °C, and in-situ XRD showed the formation of a new phase similar to cerianite (CeO_2, PDF# 43–1002) at 700 °C (Fig. 1e). However, the XRD pattern was slightly shifted from that of the pure CeO_2 reference, likely due to the significant presence of other REEs in the product. In SEM images, this product was present as aggregates with a particles size of > 50 μm and some particles on the surface had a polyhedral shape (Fig. 2b).

3.1.4. REE-doped calcite

The successful synthesis of REE-doped calcite ($CaCO_3$, PDF# 47–1743) and the presence of Y, Ce, and Nd in calcite were confirmed by XRD (Fig. 1f) and EDX (Fig. 2c), respectively. The decomposition of calcite to form lime is well studied (Tomeczek and Palugniok, 2002; Rodriguez-Navarro et al., 2009). In this study, REE-doped calcite

decomposed at 650–850 °C with a maximum at 840 °C (Fig. 3f). Correspondingly, in-situ XRD showed the coexistence of calcite and lime at 700 °C and complete transformation of calcite to lime at 1000 °C (Fig. 1f). Interestingly, during cooling, a portion of lime might have reacted with CO_2 in the air and transformed back to calcite (i.e., as evidenced by the presence of calcite (104) reflection at 3.04 Å), resulting in the coexistence of calcite and lime. Observed by SEM, the final product is mainly present as rod-shaped nanocrystals, which is completely different from the rhombohedral shape of the pristine calcite (Fig. 2c).

3.1.5. Hydrated YPO_4 and $CePO_4$

The synthesized hydrated YPO_4 and $CePO_4$ were identified as Y-churchite (YPO_4•$2H_2O$, PDF# 08–0617) and Ce-rhabdophane ($CePO_4$•H_2O, PDF# 35–0614), respectively (Fig. 1g and h). The transformation of hydrated REE phosphates to their anhydrous forms (i.e., monazite and xenotime) has been studied previously (Lucas et al., 2004a). The transformation was mainly associated with dehydration, which occurred at around 300 °C for hydrated YPO_4 and $CePO_4$ (Fig. 3g and h). For hydrated YPO_4, in-situ XRD showed the formation of xenotime at 300 °C, which persisted during subsequent heating and cooling, while hydrated $CePO_4$ completely transformed to monazite at 700 °C (Fig. 1g and h). There were no obvious morphological changes associated with the transformations as shown in Figs. 2d and S1d.

3.1.6. Apatite, monazite, xenotime, and zircon

Apatite (PDF# 09–0432), monazite (PDF# 32–0199), xenotime (PDF# 11–0254), and zircon (PDF# 06–0266) were confirmed to be pure phases by XRD (Fig. 4). Apatite ($Ca_5(PO_4)_3(OH)$) and monazite ((Ce, Nd)PO_4) were relatively enriched in LREEs (with Ce, La, and Nd being detected by EDX), while xenotime (Y, PO_4) was enriched in HREEs (with Y and Dy being detected) (Fig. S2). Zircon ($ZrSiO_4$), on the other hand, did not contain EDX-detectable REEs, but generally HREEs are more enriched in zircon because the cation radii of HREEs are closer to that of Zr^{4+} (Hoskin and Schaltegger, 2003).

The apatite sample tested in this study was very stable upon heating. As for TGA-DSC measurements, the weight loss was about 1.2 wt% at up to 1500 °C with no obvious endothermic or exothermic peaks (Fig. 5). Additionally, no obvious mineralogical changes were observed as shown by in-situ XRD (Fig. 4a). However, SEM showed some melting features on the mineral surface (Fig. S2a, pointed by arrows), likely due to the loss of anions during heating (Tonsuaadu et al., 2011). Monazite, xenotime, and zircon are typically considered to be stable during coal combustion, since their melting temperatures are generally higher than the coal combustion temperature: monazite and xenotime melt at temperature > 2000 °C (Boatner, 2002), and zircon melts at temperature > 1690 °C (Finch and Hanchar, 2003). In this study, no obvious weight loss or heat flow was observed for these three phases during heating (Fig. 5). Consistently, there were no evident mineralogical and morphological changes observed (Figs. 4 and S2).

3.2. XANES

Y K-edge and Ce L_{III}-edge XANES spectra of REE-bearing phases before and after TGA-DSC are shown in Fig. 6. Spectra of Y_2O_3, $CeCl_3$, CeO_2, and $Ce(SO_4)_2$ are also included for comparison. For the pristine REE-bearing phases (black lines), the Y K-edge spectra of REE-lignin, REE-chitosan, hydrated $Y_2(CO_3)_3$, and bastnäsite were similar to each other, with a single peak at around 17056.5 eV. However, Y K-edge XANES spectra of REE-doped calcite, hydrated YPO_4, monazite, xenotime, apatite, zircon, and Y_2O_3 showed a peak at 17056.5 eV and a shoulder at 17066 eV, but the relative intensities were different. As shown by the Ce reference compounds, Ce L_{III}-edge XANES spectra of the Ce(III)-containing phases are dominated by a single peak at 5726.5 eV (e.g., $CeCl_3$) arising from the $2p_{3/2} \rightarrow (4f^1)5d$ transition

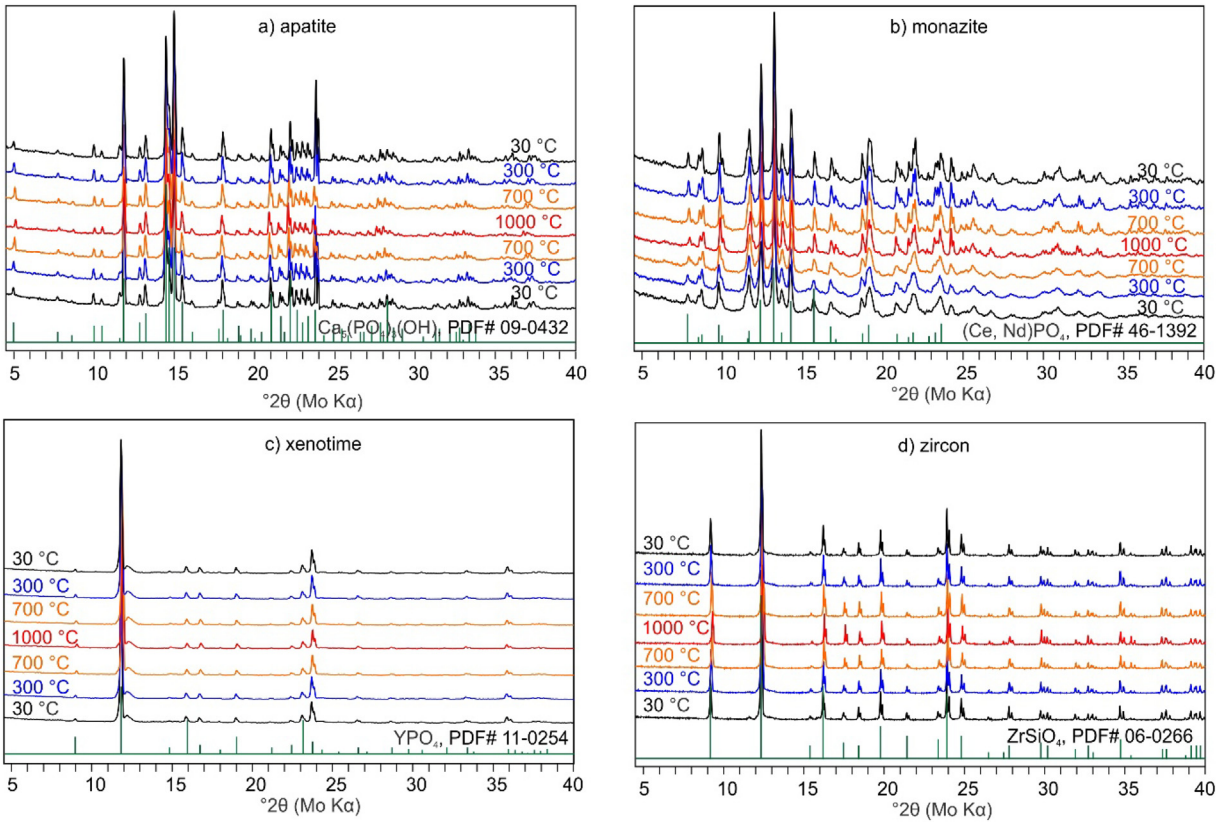

Fig. 4. In-situ XRD patterns of REE-bearing phases during heating and cooling. In each panel, XRD patterns from bottom to top were collected at 30 °C (pristine), during heating (at 300, 700, and 1000 °C), and during cooling (at 700, 300, and 30 °C).

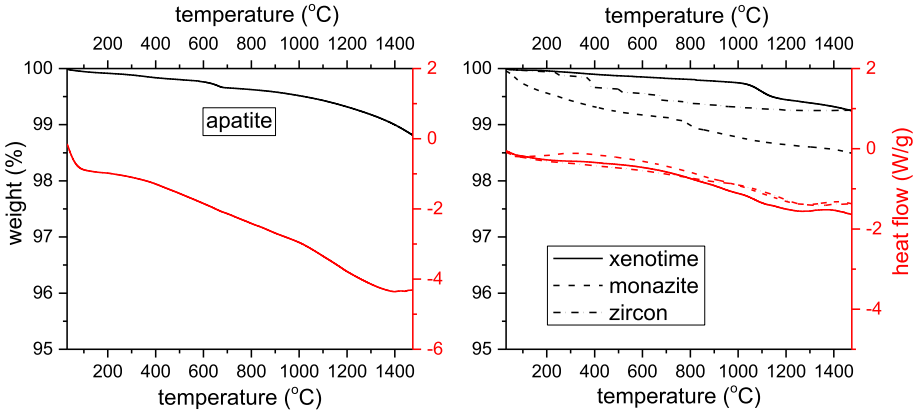

Fig. 5. TGA (black lines) and DSC (red lines) measurements of REE-bearing phases during heating: (left panel) apatite, (right panel) xenotime, monazite, and zircon. (For interpretation of the references to colour in this figure legend, the reader is referred to the web version of this article.)

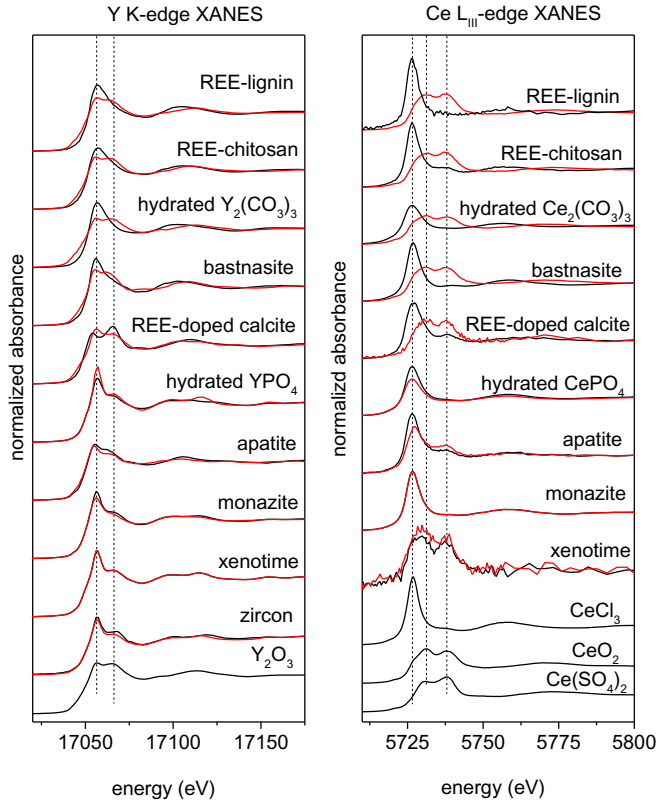

Fig. 6. Y K-edge and Ce L_{III}-edge XANES spectra of REE-bearing phases before (black lines) and after (red lines) heating to 1500 °C by TGA-DSC. Spectra of Y_2O_3, $CeCl_3$, CeO_2, and $Ce(SO_4)_2$ were plotted for comparison. Ce XANES spectrum of zircon was not obtained due to low Ce concentration in this zircon sample. (For interpretation of the references to colour in this figure legend, the reader is referred to the web version of this article.)

(Takahashi et al., 2000), whereas the XANES spectra of Ce(IV)-containing phases (e.g., CeO_2 and $Ce(SO_4)_2$) are composed of two peaks (Fig. 6). The first peak at 5731 eV corresponds to the $2p_{3/2} \rightarrow (4f^1L)5d$ transition and the second peak at 5738 eV is due to the $2p_{3/2} \rightarrow (4f^0)5d$ transition (Takahashi et al., 2000). For the pristine REE-bearing phases (black lines), their Ce XANES spectra all showed a single peak at 5726.5 eV (except for xenotime), suggesting the dominant presence of Ce(III) in these phases. In marked contrast, the Ce XANES spectrum of xenotime was characterized with two peaks at 5729 and 5738 eV, implying the dominant presence of Ce(IV) in xenotime. Ce spectrum of zircon was not obtained likely due to the low concentration of Ce in this zircon sample.

Compared to the pristine REE-bearing phases, the XANES spectra after heating up to 1500 °C displayed varied degrees of spectral changes (Fig. 6). The Y K-edge XANES spectra of REE-lignin, REE-chitosan, hydrated $Y_2(CO_3)_3$, bastnäsite, REE-doped calcite, and hydrated YPO_4 after heating were distinct from their spectra before heating, consistent with the mineralogical changes of these phases as shown by in-situ XRD (Fig. 1). Meanwhile, the Ce L_{III}-edge XANES spectra of REE-lignin, REE-chitosan, hydrated $Ce_2(CO_3)_3$, bastnäsite, and REE-doped calcite after heating were characterized with two peaks at 5731 and 5738 eV, indicating the oxidation of Ce(III) to Ce(IV) during phase transformation. In contrast, although hydrated $CePO_4$ transformed to monazite after heating, both the Ce XANES spectra before and after heating showed a single peak at 5726.5 eV, indicating no obvious Ce oxidation associated with this transformation. Apatite, monazite, xenotime, and zircon barely changed as shown by in-situ XRD (Fig. 4) and TGA-DSC (Fig. 5). However, the Y XANES spectra of apatite, monazite, and zircon after heating were different from the pristine spectra (before heating), all displaying a featureless white line at 17056.5 and 17066 eV and broadened oscillations at 17100–17175 eV. Such spectral changes might be associated with more disordered local structure of Y after heating. Additionally, the Ce XANES spectra of monazite and xenotime after heating were similar to the pristine spectra, while the Ce XANES spectrum of apatite after heating showed decreasing peak intensity at 5728 eV and increasing peak intensity at 5738 eV, suggesting partial oxidation of Ce during the heating of apatite.

4. Discussion

4.1. REE behaviors during coal combustion

In this study, complementary TGA-DSC, in-situ XRD, SEM-EDX, and XAS analyses provided systematic characterization on the thermodynamic properties of twelve representative REE-bearing phases during heating. These REE-bearing phases can be divided into three groups based on their behaviors during heating (Table 1):

(1) Group 1 includes REE-lignin and REE-chitosan complexes, hydrated $Y_2(CO_3)_3$ and $Ce_2(CO_3)_3$, bastnäsite, and REE-doped calcite, which decomposed and formed corresponding oxides with Ce(III) oxidization at temperatures well below 1000 °C;
(2) Group 2 includes hydrated YPO_4 and $CePO_4$, which formed corresponding anhydrous REE phosphates without obvious Ce(III) oxidation;
(3) Group 3 includes apatite, monazite, xenotime, and zircon, which barely altered during heating up to 1500 °C, although Y local structure became more disordered in apatite, monazite, and zircon,

and Ce(III) in apatite was partially oxidized.

Based on the results from this study, if REE-organic complexes, REE carbonates (including hydrated REE carbonates and bastnäsite), and REE-bearing carbonates are present in coal, they would decompose and Ce would oxidize during coal combustion, and finally occur as REE oxides or REE-bearing oxides (e.g., lime) in CA. Such findings are consistent with previous studies on REE speciation in CA at both micro and bulk scales. At the micro scale, for example, REE oxides (Montross et al., 2018) and REE-bearing lime in CA (Liu et al., 2019) have been observed using SEM-EDX, and 10-μm Ce(IV) oxides have also been identified using synchrotron X-ray spectromicroscopy (Stuckman et al., 2018). At the bulk scale, REE-organic complexes are estimated to account for ~25% of total REEs in coal (Lin et al., 2017), therefore, it is reasonable to expect that REE oxides would be a significant fraction in CA if the abovementioned transformations occur during coal combustion. Indeed, both chemical extraction methods (e.g., acid leaching and sequential extraction) and linear combination fitting of XANES data showed that REE oxides might account for 10–60% of total REEs in CA (Taggart et al., 2018; Liu et al., 2019).

On the other hand, REE phosphates and REE-bearing phosphate (e.g., apatite) and silicate minerals (e.g., zircon) might remain in CA because of their high stability as shown in this study. Indeed, REE phosphates, apatite, and zircon were commonly observed in previous studies (e.g., Hower et al., 2018; Montross et al., 2018; Liu et al., 2019), confirming their retention during coal combustion. However, several previous studies have also shown that those REE-bearing phases might decompose at some degrees during combustion. For example, shattering and size reduction of monazite after heating up to 1400 °C have been observed (Hood et al., 2017). In addition, zircon and monazite with decomposition features such as spherical shape and melting holes were previously observed by SEM (Liu et al., 2019). The reason that we did not observe these features by SEM in this study might be due to the limitations of the current experimental setup, since the highest heating temperature (1500 °C) in this study was slightly lower than some boiler temperatures (1200–1800 °C), and TGA-DSC and in-situ XRD cannot mimic the rapid heating and quenching processes during coal combustion. Alternatively, the decomposition of these phases might also be due to the coexistence of other components in coal, such as lime (CaO, derived from calcite decomposition). For example, it was found that the presence of CaO could significantly lower the melting temperature of monazite to 600–700 °C and lead to the formation of REE oxides and $Ca_3(PO_4)_2$ (Hikichi et al., 1997; Wu et al., 2007).

In addition, newly-formed REE oxides and REE-bearing oxides might further diffuse and mix with other phases during combustion, such as aluminosilicate glass phase, resulting in dispersed REEs throughout glass phase (e.g., Kolker et al., 2017; Stuckman et al., 2018; Liu et al., 2019). REE phosphates, apatite, and zircon that retain during combustion might occur as discrete particles or encapsulated REE-bearing phases in glass (e.g., Hower et al., 2018; Stuckman et al., 2018; Liu et al., 2019). Because our experimental conditions could not fully mimic the flue gas composition, it is hard to explore potential reactions between REEs and flue gas. However, it is worth noting that some newly-formed lime reacted with CO_2 and transferred back to calcite during cooling as shown by XRD (Fig. 1f), but this is not the case for REE oxides (Figs. 1a, b, c, and d). Considering that CO_2 is the most dominant phase of flue gas, REEs might react with flue gas (such as CO_2) during cooling, though the extent might be minor.

4.2. Utilization of XAS analysis

XAS is a powerful technique for characterizing metal speciation in complex environmental matrices such as coal and CA. Previous studies have utilized XANES to identify and quantify the speciation of REEs in CA (Stuckman et al., 2018; Taggart et al., 2018; Liu et al., 2019). In this study, REE local structure and oxidation state of representative REE-bearing phases after heating was analyzed and compared with the pristine ones using Y and Ce XANES. Due to the mineralogical transformations of REE-bearing phases after heating (such as REE-organic complex, REE carbonates, and REE-bearing carbonates), their Y and Ce XANES spectra were distinct from the pristine spectra (Fig. 6), showing changes of REE local structure and oxidation of Ce(III) after heating (Figs. 1 and 3). In marked contrast, REE local structure and oxidation state in apatite, monazite, xenotime, and zircon barely altered after heating (Figs. 4, 5, and 6). Moreover, it is worth noting that Y spectral difference still existed even for heated products with the same mineralogy. For examples, although both hydrated $Y_2(CO_3)_3$ and REE-lignin transformed to Y_2O_3 after heating, their Y spectra were different in the shoulder peak position. The shoulder peak of the Y_2O_3 from hydrated $Y_2(CO_3)_3$ after heating was located at 17065.5 eV, while it shifted to 17064.5 eV for the Y_2O_3 from REE-lignin after heating (see Fig. S3 for comparison). Such spectral differences were likely due to the significant presence of other REEs (e.g., Ce and Nd) in Y_2O_3 from REE-lignin after heating. The co-existence of other REEs in REE-bearing phases might also explain the spectra differences between products from REE-chitosan and bastnäsite after heating and between products from hydrated YPO_4 and xenotime after heating (Fig. S3).

Previous studies have utilized linear combination fitting (LCF) of Y XANES spectra to identify and quantify REE speciation in CA, but several issues still remain (Taggart et al., 2018; Liu et al., 2019). For example, REE oxides and REE phosphates have been identified as the main REE species in CA using LCF of Y XANES data, accounting for a total of > 60% REE species in CA. However, it is difficult to accurately identify and quantify the relative percentages of the remaining REE species (Liu et al., 2019). Based on the results from this current study, the significant presence of REE oxides and REE phosphates in CA is reasonable and likely due to the formation of REE oxides after heating and the retention of REE phosphates, respectively (Section 4.1). The difficulties associated with identifying/differentiating the remaining REE species is possibly due to the intrinsic limitation of the LCF method as well as the selection of REE reference compounds. LCF is a mathematic method with a generally agreed fitting error range of ~10%. In addition, considering the co-existence of different REEs in one species, as well as the mineralogical and local structural changes of REE-bearing phases during coal combustion, pure and intact REE reference compounds as used in previous studies (Taggart et al., 2018; Liu et al., 2019) might not fully represent the combusted products, resulting in further uncertainties in species identification and quantification, especially toward the minor species. Therefore, based on our current results on the final products/structures of combusted REE-bearing phases, we recommend including Y_2O_3, cerianite, lime, apatite, monazite, xenotime, and zircon as reference compounds for LCF of XANES data for the identification and quantification of REE species in CA. Further, if elemental concentration and data quality allow, LCF of the extended X-ray absorption fine structure (EXAFS) data might be also used to complement LCF of XANES data. Taken together, mineralogical transformations of REE speciation and corresponding representative REE reference compounds should be considered in the interpretation of XAS data and it would be better to cross-validated XAS data with other techniques (e.g., chemical leaching) to provide more reliable interpretation.

5. Conclusions

In order to investigate the mineralogy, structure, and oxidation state changes of representative REE-bearing phases during coal burning process and better understand the REE speciation in CA, twelve REE-bearing phases were subjected to heating up to 1500 °C by TGA-DSC and up to 1000 °C by in-situ XRD. The products after heating were characterized by SEM-EDX and their local structure and oxidation state were investigated by XANES. It is found that:

(1) REE-organic complexes, REE carbonates, and REE-bearing

carbonates transformed to corresponding oxides after heating, accompanied with Ce(III) oxidation;
(2) Hydrated REE phosphates formed corresponding anhydrous REE phosphates after heating with no evident Ce(III) oxidation;
(3) Apatite, monazite, xenotime, and zircon barely altered during heating, although Ce(III) in apatite was partially oxidized and Y local structure became more disordered in apatite, monazite, and zircon.

Our results provided an in-depth understanding on REE behaviors during coal combustion, including potential mineral transformations of REE-organic complexes and REE carbonate minerals, as well as the retention of REE phosphate and silicate minerals. It may also provide guidance on the exploration of proper pretreatment techniques (e.g., calcinations) for improving REE recovery from coal. Due to the co-existence of REEs and mineralogical and local structural changes of REE-bearing phases during combustion, uncertainties might be introduced during LCF analysis of REE XANES spectra, and XAS data should be interpreted with caution and cross-validated by other techniques.

Declaration of Competing Interest

The authors declare that they have no known competing financial interests or personal relationships that could have appeared to influence the work reported in this paper.

Acknowledgements

This work was supported by the U.S. National Science Foundation [grants number 1739884 and 1605692] and Department of Energy (DOE) [grant number DE-FE0031739]. The authors appreciate the constructive comments and suggestions from the reviewers. Portions of this study were conducted at the Advanced Photon Source (APS) and Stanford Synchrotron Radiation Lightsource (SSRL). APS is a U.S. Department of Energy (DOE) Office of Science User Facility operated for the DOE Office of Science by Argonne National Laboratory under Contract No. DE-AC02-06CH11357. Use of SSRL, SLAC National Accelerator Laboratory, is supported by DOE Office of Science, Office of Basic Energy Sciences under Contract No. DE-AC02-76SF00515.

Appendix A. Supplementary data

Supplementary data to this article can be found online at https://doi.org/10.1016/j.coal.2019.103371.

References

Blissett, R., Smalley, N., Rowson, N., 2014. An investigation into six coal fly ashes from the United Kingdom and Poland to evaluate rare earth element content. Fuel 119, 236–239.
Boatner, L.A., 2002. Synthesis, structure, and properties of monazite, pretulite, and xenotime. Rev. Mineral. Geochem. 48, 87–121.
Dai, S., Finkelman, R.B., 2018. Coal as a promising source of critical elements: progress and future prospects. Int. J. Coal Geol. 186, 155–164.
Dai, S., Zhao, L., Hower, J.C., Johnston, M.N., Song, W., Wang, P., Zhang, S., 2014. Petrology, mineralogy, and chemistry of size-fractioned fly ash from the Jungar power plant, Inner Mongolia, China, with emphasis on the distribution of rare earth elements. Energy Fuel 28, 1502–1514.
Fedorov, P., Il'in, N., 2012. Yttrium carbonate thermolysis. Russ. J. Inorg. Chem. 57, 237–241.
Finch, R.J., Hanchar, J.M., 2003. Structure and chemistry of zircon and zircon-group minerals. Rev. Mineral. Geochem. 53, 1–25.
Franus, W., Wiatros-Motyka, M.M., Wdowin, M., 2015. Coal fly ash as a resource for rare earth elements. Environ. Sci. Pollut. Res. 22, 9464–9474.
Goodarzi, F., 1984. Chitinous fragments in coal. Fuel 63, 1504–1507.
Granite, E.J., Pennline, H.W., 2002. Photochemical removal of mercury from flue gas. Ind. Eng. Chem. Res. 41, 5470–5476.
Hatcher, P.G., Breger, I.A., Szeverenyi, N., Maciel, G.E., 1982. Nuclear magnetic resonance studies of ancient buried wood—II. Observations on the origin of coal from lignite to bituminous coal. Org. Geochem. 4, 9–18.
Hikichi, Y., Ota, T., Hattori, T., 1997. Thermal, mechanical and chemical properties of sintered monazite-(La, Ce, Nd or Sm). Mineral. J. 19, 123–130.
Hood, M.M., Taggart, R.K., Smith, R.C., Hsu-Kim, H., Henke, K.R., Graham, U., Groppo, J.G., Unrine, J.M., Hower, J.C., 2017. Rare Earth Element distribution in Fly Ash Derived from the Fire Clay Coal, Kentucky. Coal Combust. Gasification Prod. 9, 22–33.
Hoskin, P.W., Schaltegger, U., 2003. The composition of zircon and igneous and metamorphic petrogenesis. Rev. Mineral. Geochem. 53, 27–62.
Hower, J.C., Qian, D., Briot, N.J., Henke, K.R., Hood, M.M., Taggart, R.K., Hsu-Kim, H., 2018. Rare earth element associations in the Kentucky State University stoker ash. Int. J. Coal Geol. 189, 75–82.
Kolker, A., Scott, C., Hower, J.C., Vazquez, J.A., Lopano, C.L., Dai, S., 2017. Distribution of rare earth elements in coal combustion fly ash, determined by SHRIMP-RG ion microprobe. Int. J. Coal Geol. 184, 1–10.
Laudal, D.A., Benson, S.A., Addleman, R.S., Palo, D., 2018. Leaching behavior of rare earth elements in fort union lignite coals of North America. Int. J. Coal Geol. 191, 112–124.
Liang, Y., Liu, Y., Lin, R., Guo, D., Liao, C., 2016. Leaching of rare earth elements from waste lamp phosphor mixtures by reduced alkali fusion followed by acid leaching. Hydrometallurgy 163, 99–103.
Lin, R., Bank, T.L., Roth, E.A., Granite, E.J., Soong, Y., 2017. Organic and inorganic associations of rare earth elements in central Appalachian coal. Int. J. Coal Geol. 179, 295–301.
Liu, P., Huang, R., Tang, Y., 2019. Comprehensive understandings of Rare Earth Element (REE) speciation in coal fly ashes and implication for REE extractability. Environ. Sci. Technol. 53, 5369–5377.
Long, K.R., Van Gosen, B.S., Foley, N.K., Cordier, D., 2012. The principal rare earth elements deposits of the United States: A summary of domestic deposits and a global perspective. In: Non-Renewable Resource Issues. Springer, pp. 131–155.
Lucas, S., Champion, E., Bernache-Assollant, D., Leroy, G., 2004a. Rare earth phosphate powders RePO4· nH2O (Re= La, Ce or Y) II. Thermal behavior. J. Solid State Chem. 177, 1312–1320.
Lucas, S., Champion, E., Bregiroux, D., Bernache-Assollant, D., Audubert, F., 2004b. Rare earth phosphate powders REPO4· NH2O (Re= La, Ce or Y)—Part i. Synthesis and characterization. J. Solid State Chem. 177, 1302–1311.
Maes, S., Zhuang, W.-Q., Rabaey, K., Alvarez-Cohen, L., Hennebel, T., 2017. Concomitant leaching and electrochemical extraction of rare earth elements from monazite. Environ. Sci. Technol. 51, 1654–1661.
Miyawaki, R., Matsubara, S., Yokoyama, K., Takeuchi, K., Terada, Y., Nakai, I., 2000. Kozoite-(Nd), Nd (CO3)(OH), a new mineral in an alkali olivine basalt from Hizen-cho, Saga Prefecture, Japan. Am. Mineral. 85, 1076–1081.
Montross, S.N., Verba, C.A., Chan, H.L., Lopano, C., 2018. Advanced characterization of rare earth element minerals in coal utilization byproducts using multimodal image analysis. Int. J. Coal Geol. 195, 362–372.
Padeste, C., Cant, N.W., Trimm, D.L., 1994. Thermal decomposition of pure and rhodium impregnated cerium (III) carbonate hydrate in different atmospheres. Catal. Lett. 24, 95–105.
Park, D.M., Brewer, A., Reed, D.W., Lammers, L.N., Jiao, Y., 2017. Recovery of Rare Earth Elements from low-grade feedstock leachates using engineered bacteria. Environ. Sci. Technol. 51, 13471–13480.
Peniche-Covas, C., Argüelles-Monal, W., San Román, J., 1993. A kinetic study of the thermal degradation of chitosan and a mercaptan derivative of chitosan. Polym. Degrad. Stab. 39, 21–28.
Quann, R.J., Neville, M., Janghorbani, M., Mims, C.A., Sarofim, A.F., 1982. Mineral matter and trace-element vaporization in a laboratory-pulverized coal combustion system. Environ. Sci. Technol. 16, 776–781.
Ravel, B., Newville, M., 2005. ATHENA, ARTEMIS, HEPHAESTUS: data analysis for X-ray absorption spectroscopy using IFEFFIT. J. Synchrotron Radiat. 12, 537–541.
Rodriguez-Navarro, C., Ruiz-Agudo, E., Luque, A., Rodriguez-Navarro, A.B., Ortega-Huertas, M., 2009. Thermal decomposition of calcite: Mechanisms of formation and textural evolution of CaO nanocrystals. Am. Mineral. 94, 578–593.
Seredin, V.V., Dai, S., 2012. Coal deposits as potential alternative sources for lanthanides and yttrium. Int. J. Coal Geol. 94, 67–93.
Stuckman, M., Lopano, C., Granite, E., 2018. Distribution and speciation of rare earth elements in coal combustion by-products via synchrotron microscopy and spectroscopy. Int. J. Coal Geol. 195, 125–138.
Taggart, R.K., Hower, J.C., Dwyer, G.S., Hsu-Kim, H., 2016. Trends in the rare earth element content of US-based coal combustion fly ashes. Environ. Sci. Technol. 50, 5919–5926.
Taggart, R.K., Rivera, N.A., Levard, C., Ambrosi, J.-P., Borschneck, D., Hower, J.C., Hsu-Kim, H., 2018. Differences in bulk and microscale yttrium speciation in coal combustion fly ash. Environ. Sci.: Processes Impacts 20, 1390–1403.
Takahashi, Y., Shimizu, H., Usui, A., Kagi, H., Nomura, M., 2000. Direct observation of tetravalent cerium in ferromanganese nodules and crusts by X-ray-absorption near-edge structure (XANES). Geochim. Cosmochim. Acta 64, 2929–2935.
Tang, Y., Elzinga, E.J., Lee, Y.J., Reeder, R.J., 2007. Coprecipitation of chromate with calcite: batch experiments and X-ray absorption spectroscopy. Geochim. Cosmochim. Acta 71, 1480–1493.
Tomeczek, J., Palugniok, H., 2002. Kinetics of mineral matter transformation during coal combustion. Fuel 81, 1251–1258.
Tonsuaadu, K., Gross, K.A., Plūduma, L., Veiderma, M., 2011. A review on the thermal stability of calcium apatites. J. Therm. Anal. Calorim. 110, 647–659.
Wall, T., Liu, Y., Spero, C., Elliott, L., Khare, S., Rathnam, R., Zeenathal, F., Moghtaderi, B., Buhre, B., Sheng, C., 2009. An overview on oxyfuel coal combustion—state of the art research and technology development. Chem. Eng. Res. Des. 87, 1003–1016.
Wood, S.A., 1993. The aqueous geochemistry of the rare-earth elements: critical stability constants for complexes with simple carboxylic acids at 25° C and 1 bar and their application to nuclear waste management. Eng. Geol. 34, 229–259.
Wu, W.-Y., Xue, B., Wu, Z.-Y., Sun, S.-C., Tu, G.-F., 2007. Reaction process of monazite and bastnaesite mixed rare earth minerals calcined by CaO-NaCl-CaCl2. Trans. Nonferrous Metals Soc. China 17, 864–868.
Zhang, W., Honaker, R., 2019. Calcination pretreatment effects on acid leaching characteristics of rare earth elements from middlings and coarse refuse material associated with a bituminous coal source. Fuel 249, 130–145.